Structural Properties of the Amorphous Ices: An Analysis in Terms of Distance-Ranked Neighbors and Angular Correlations[†]

A. Marco Saitta,* Thierry Strässle, and Stefan Klotz

Physique des Milieux Denses, Institut de Minéralogie et Physique des Milieux Condensés, CNRS-UMR 7590, Université Pierre et Marie Curie, F-75252 Paris, France

In this work we study through computer simulations the three known forms of amorphous ice, namely, the low density (LDA), the high density (HDA), and the very high density (VHDA) amorphous ices, at various pressures and temperatures. Adopting the TIP4P model, we are able to reproduce these three forms by following experiment-like procedures. Those systems are characterized from thermodynamic and structural points of view, in particular through an insightful analysis of the behavior of the second-shell neighbors in the various stages of the simulations. The distance-ranked neighbors are found to be the relevant markers of the differentiation mechanisms of the three forms, since their response to pressure induces specific distortions of the orientational correlations. We show that LDA, HDA, and VHDA are disordered forms whose local structures tend to a single tetrahedral network, to an ice-VII-like arrangement, and to a random-close-packed simple liquidlike structure, respectively. Despite the major structural deformations induced by pressure, the hydrogen bonds are still present in each of those forms, even though deformations of the tetrahedral angles are necessary to adapt to the denser structures.

I. Introduction

The experimental evidence of three distinct forms of amorphous ice has spurred great interest and a large amount of experimental[1−5] and theoretical[6−13] work, also in conjunction with the postulated liquid−liquid first-order phase transition in the supercooled regime.[14−19] The high-density amorphous (HDA) form can be obtained by compressing ordinary ice I_h at 77 K up to about 1 GPa and is recovered at ambient pressure at a density of about 1.17 g/ml.[20,21] This recovered form transforms into a different disordered form, named low-density amorphous (LDA) ice, when heated beyond 115 K.[22,23] The transformation between these two forms can be also induced by pressure at 130 K, and it shows a clear first-order nature.[24] A third amorphous form was obtained when HDA was heated to 170 K at 1.1 GPa and then cooled back to 80 K.[25] In this case the system obtained at the end of this procedure is denser, and thus labeled very high-density amorphous (VHDA) ice, and follows a different equation of state along the downstroke with respect to HDA. Its recovered density at ambient pressure is about 7% larger than the HDA density. The existence of two high-density forms and their thermodynamic and structural relations have been a topic of great interest and debate in the past few years. In particular, it has been recently demonstrated[12] that VHDA represents a "disordered limit" of the dense amorphous forms that does not involve the significant re-arrangement of the hydrogen bonds necessary to form two interpenetrating networks, as in the high-density crystalline phases (ice VII, ice VIII, and ice X). In fact, the structure of high-pressure VHDA is described as tending toward a random close-packed (rcp) structure yet compatible with H-bonds, characterized by a significant angular distortion of the first-neighbors tetrahedral cage. Such topological differentiation of

VHDA from HDA is due to the high-pressure annealing of the HDA sample to 160 K, which allows a group of second neighbors to move *outward* at increasing density, making the rcp arrangement possible.[13]

In this paper we report a theoretical study in which molecular dynamics (MD) calculations have been carried out on the amorphous ices following the experimental procedures in order to fully characterize LDA, HDA, and VHDA from the structural point of view and to shed light on the mechanisms determining the molecular arrangements characteristic of each form. We will first present their pair distribution functions (PDFs) throughout all the pressure range considered in our study, showing however that only limited information can be extracted from them. The central part of our work concerns our analysis in terms of the instantaneous neighbors of each molecule, ranked according to their distance. We will show that this simple tool allows a much deeper understanding of the different transformation steps occurring at the different conditions of pressure, temperature, and density. This approach is even more insightful when those distances are scaled with respect to the homogeneous variations of the volume, since it underlines the "net" displacements of specific subgroups of neighbors in correspondence to the structural transformations. The inclusion of the orientational correlations completes our study, allowing us to understand the local structure of the amorphous ices. The paper is organized as follows: in section 2 we will describe our calculations, and the thermodynamic path we have followed in order to obtain the different forms of amorphous ices; in section 3 we will present the thermodynamic properties of our systems in terms of enthalpy and the structural characterizations in terms of pair correlation functions. In section 4 we will analyze the different ices through the characterization of the instantaneous distance-ranked neighbors of a given molecule; in section 5 these results will be discussed in terms of angular correlations. The last section will be devoted to conclusions and perspectives.

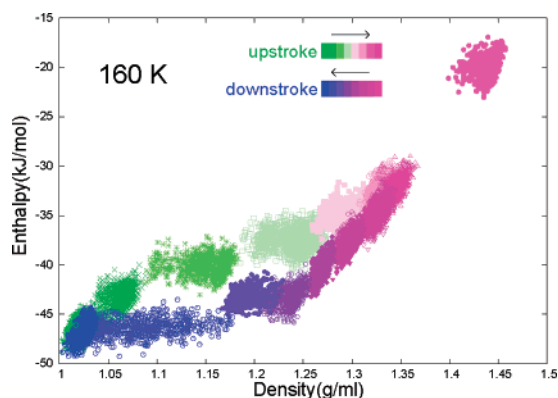* To whom correspondence may be addressed. E-mail: ms@pmc.jussieu.fr.

Figure 1. Instantaneous enthalpy at 160 K along the upstroke and the downstroke. As indicated by the arrows, along the upstroke the system evolves from green to magenta, while along the downstroke it changes from magenta at high pressure to blue at ambient pressure.

II. Method

Our MD calculations have been performed in the NPT ensemble in the 0−2 GPa pressure range. We employed supercells containing 512 H_2O molecules and the TIP4P potential for water.[26] Our simulation times at each pressure were in the 4.0−20.0 ns range. We chose to start our simulation from LDA, obtained by slowly cooling the liquid phase through a simulated annealing technique, whose structure is found to be very similar to other reported data on LDA obtained from heating HDA.[8] On the other hand, HDA is known to have a much more significant structural variability, dependent on the different procedures through which it is obtained and on the pressures and temperatures to which the HDA sample has been subjected.

Multi-nanosecond-long simulations have then been carried out at ambient pressure and then at 0.2, 0.4, 0.6, 0.8, 1.0, 1.5, and 2.0 GPa. Once at 2.0 GPa, the system was decompressed to ambient pressure, through simulations at the same pressure steps as in the upstroke, while the temperature was kept constant at 80 K. We will refer to this protocol as the "HDA procedure". In parallel, a replica of the system at 2.0 GPa and 80 K was heated to 160 K, then slowly cooled back to 80 K, and then decompressed at constant temperature following the same downstroke steps as in the HDA procedure. This protocol will be referred to as the "VHDA procedure". Similar upstroke/downstroke simulations at constant temperature have been performed at 130 and 160 K.

III. Thermodynamics and Pair Distribution Functions

The thermodynamics of the system was followed by calculating the instantaneous enthalpy $H(t) = E(t) + P(t)V(t)$, obtained from the direct calculation of the internal energy E, the pressure P, and the volume V. In Figure 1 we show the enthalpy of the system at 160 K as a function of the instantaneous density along the upstroke and the downstroke. Since the simulations are performed at discrete pressure steps, as described above, the results appear in groups of points corresponding to individual simulations at a given pressure and distinct colors in all figures. The figure shows that the system densifies in an apparently continuous way upon pressure and that the downstroke is analogously quite smooth. Interestingly, the two thermodynamic paths are close but a clear hysteresis, seemingly not due to artifacts of the calculations, can be observed between $\rho \approx 1.05$ g/ml and $\rho \approx 1.35$ g/ml. At the end of the cycle, however, the system is thermodynamically equivalent to the sample at the beginning of the upstroke.
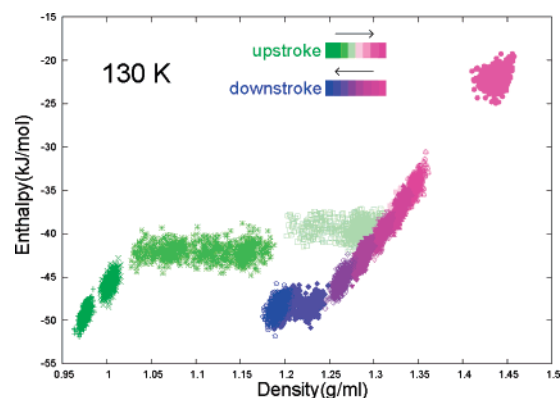

Figure 2. Instantaneous enthalpy at 130 K along the upstroke and the downstroke. The same color code as in Figure 1 is adopted.
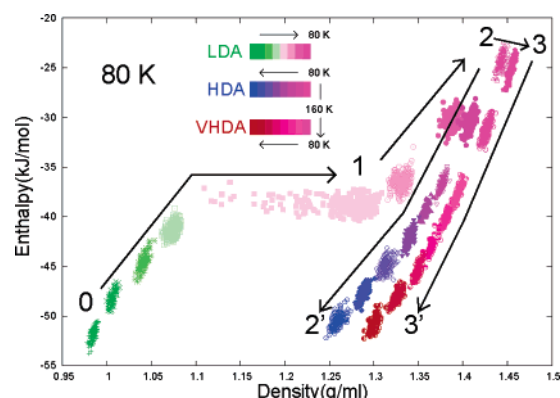

Figure 3. Instantaneous enthalpy at 80 K along the upstroke and the two downstrokes, referring to the HDA and the VHDA procedures. The numbers and the big arrows along the simulation data indicate the different stages of the protocols. In the upper central part of the figure, our color code is displayed: the little arrow pointing to the right indicates the pressure upstroke from the LDA phase, while the little arrows pointing to the left indicate the two pressure downstrokes; the little vertical arrow between the HDA and the VHDA color palettes illustrates the temperature annealing performed in the VHDA procedure.

At 130 K, as we show in Figure 2, the hysteresis is more pronounced, and the densification occurs more abruptly between 0.4 and 0.6 GPa (points depicted in light green). At this stage a very significant increase of the density is observed while the corresponding relative increase of the enthalpy is much smaller. More importantly, the downstroke ends at ambient pressure at a density of about 1.18 g/ml; that is, the system is trapped at high density and cannot revert to its initial low-density form. We note that this temperature is higher than the experimental temperature of 115 K, beyond which recovered HDA transforms into LDA.

In Figure 3 we show the enthalpy at 80 K as a function of the instantaneous density along the (common) upstroke and the two different downstrokes followed to reproduce in the simulations the HDA and the VHDA procedures. In the VHDA case, only data obtained at 80 K after the annealing at 160 K are shown. As a consequence, all data shown in the figure refer to simulations performed at the same temperature of 80 K. The analysis of the upstroke curve shows, after a compressive behavior of the LDA phase (shown in the green tones in Figure 3) up to 0.6 GPa, a dramatic increase of the density during the 0.8 GPa simulation (shown in light magenta). This abrupt densification is compatible with the occurrence of a first-order LDA−HDA phase transformation,[24] despite the relatively small box and short time scale of the simulations. This transformation is then followed by a further compression of HDA.

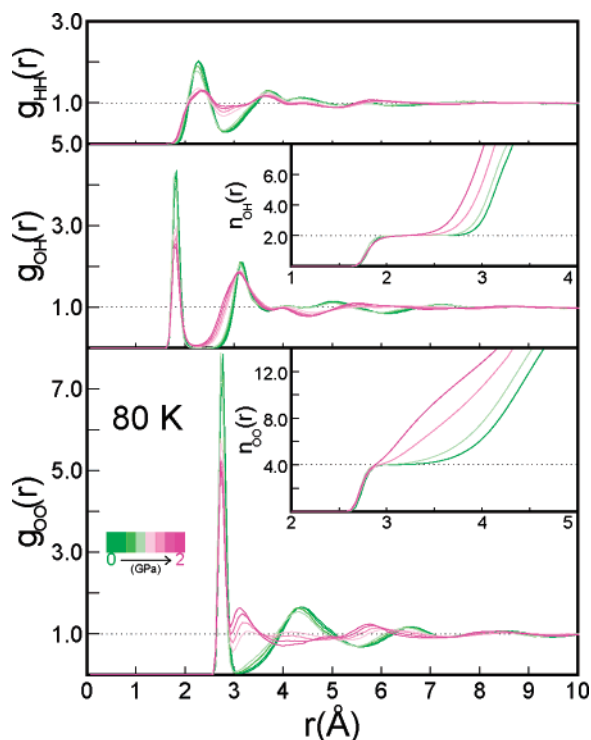**Figure 4.** Oxygen−oxygen (lower panel), oxygen−hydrogen (middle panel), and hydrogen−hydrogen intermolecular pair distribution functions at 80 K along the upstroke. The same color code as in Figure 3 is adopted. The little arrow indicates the pressure evolution from 2 GPa to 0. In the insets of the lower and the middle panels, we show the coordination numbers $n_{OO}(r)$ and $n_{OH}(r)$. The plateau of the latter one is shown at 2.0 because the additional trivial intramolecular coordination is not included in the figure.

Once the highest pressure is reached (shown in bright magenta), the system is decompressed at the same temperature following the HDA procedure. As shown in the figure (from magenta to blue) HDA follows a very different equation of state with respect to the upstroke, and it is recovered at ambient pressure at a density of about 1.25 g/ml, giving thus rise to significant hysteresis. At this stage, as at the end of the downstroke at 130 K, the enthalpy and thus the internal energy of ambient pressure HDA are slightly higher than those for LDA, but recovered HDA is kinetically trapped and thus not able to cross the barrier and revert to LDA. At 2.0 GPa the sample obtained through the VHDA procedure is slightly denser (about 1%) than the corresponding HDA. In agreement with experiments, it follows a different (lower) equation of state along decompression, to a final ambient pressure density of about 1.3 g/ml (magenta to red), about 4% larger than our recovered HDA, a difference smaller than observed experimentally.[25]

The structural characterization of disordered systems is usually achieved through the determination of the pair distribution function (PDF) $g(r)$ values. In the case of water, in particular, the oxygen−oxygen $g_{OO}(r)$ contains the two-body structural properties at the molecular level. We report in Figure 4 the three LDA intermolecular $g(r)$ values calculated at 80 K along the upstroke, as indicated by the color code, and the integrated oxygen−oxygen and oxygen−hydrogen coordination numbers. The initial LDA $g_{OO}(r)$ at ambient pressure shows the characteristic pattern of a disordered tetrahedral network, with the H-bond first sharp peak at about 2.8 Å, and the secondary peaks at 4.4, 6.6, and 8.5 Å. The $g_{OH}(r)$ and $g_{HH}(r)$, where we do not include the rigid-molecule intramolecular peaks, analogously present the characteristic features of the
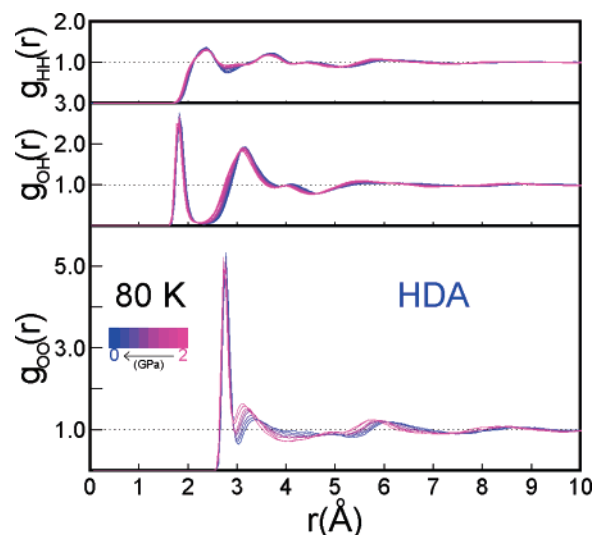

Figure 5. Oxygen−oxygen (lower panel), oxygen−hydrogen (middle panel), and hydrogen−hydrogen intermolecular pair distribution functions at 80 K along the HDA downstroke. The same color code as in Figure 3 is adopted. The little arrow indicates the pressure evolution from 2 GPa to 0.

hydrogen-bond network, particularly in the H-bond peak of the $g_{OH}(r)$ at 1.8 Å. Up to 0.6 GPa (shown in light green), very few changes are observed in all the $g(r)$ values. At a pressure of 0.8 GPa (light magenta), corresponding to the sudden density increase observed in Figure 3, a dramatic change in the oxygen−oxygen PDF occurs beyond the first H-bond peak. The intensity of the second peak beyond 4.0 Å drops, while a new peak suddenly appears at about 3.3 Å, a weak feature develops around 4.9 Å, and the low-density third peak shifts to about 5.8 Å. As pressure increases up to 2.0 GPa (bright magenta), one can observe how the low-density secondary peak has become a minimum, while the new features are all enhanced, but without any other significant qualitative modification. Inspection of the other $g(r)$ values confirms that a major structural change occurs at 0.8 GPa, reflected in a different shape of the low-density peaks and in new features of the $g_{OH}(r)$ beyond 4.0 Å. The $n_{OO}(r)$ and $n_{OH}(r)$, reported in the insets, show however that the H-bond network is still intact and that the coordination number of a given molecule is still very close to 4.0.

In Figure 5 we report the PDFs at 80 K along the downstroke to obtain, at ambient pressure, the HDA form. The $g_{OO}(r)$ shows that the system maintains a structure very similar to the one at high pressure, with minor outward shifts and intensity decrease of the secondary features. The $g_{OH}(r)$ and $g_{HH}(r)$ are practically unchanged. In Figure 6 we display the PDFs, at 80 K, obtained after the annealing at 160 K and along the downstroke to ambient pressure VHDA, following the VHDA procedure. In this case, as in the case of HDA, only minor shifts are observed in the $g_{OO}(r)$ and almost none at all in the other ones.

To clarify the structural differences that could somehow justify the experimental and theoretical observations of two distinct high-density forms of amorphous ice, we compare in Figure 7 the PDFs of LDA, HDA, and VHDA at ambient pressure. One can observe that, while both HDA and VHDA are very different from LDA in terms of PDFs, the structural difference between the high-density forms is less significant: we observe a more intense feature of VHDA around 3.3 Å and a less intense one around 4.1 Å. Interestingly, the ambient pressure PDF of VHDA is more similar, but not identical, to the PDF of HDA at about 0.6 GPa along the downstroke, in good agreement with experimental observations.[27] These minor
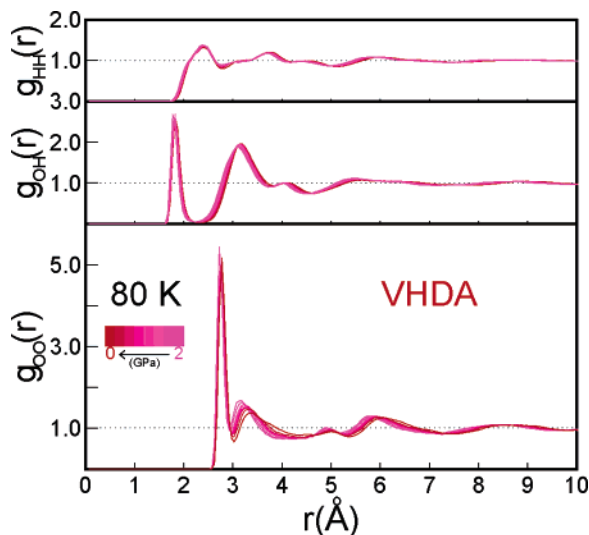
Figure 6. Oxygen−oxygen (lower panel), oxygen−hydrogen (middle panel), and hydrogen−hydrogen intermolecular pair distribution functions at 80 K after the annealing at 160 K and along the VHDA downstroke. The same color code as in Figure 3 is adopted. The little arrow indicates the pressure evolution from 2 GPa to 0.
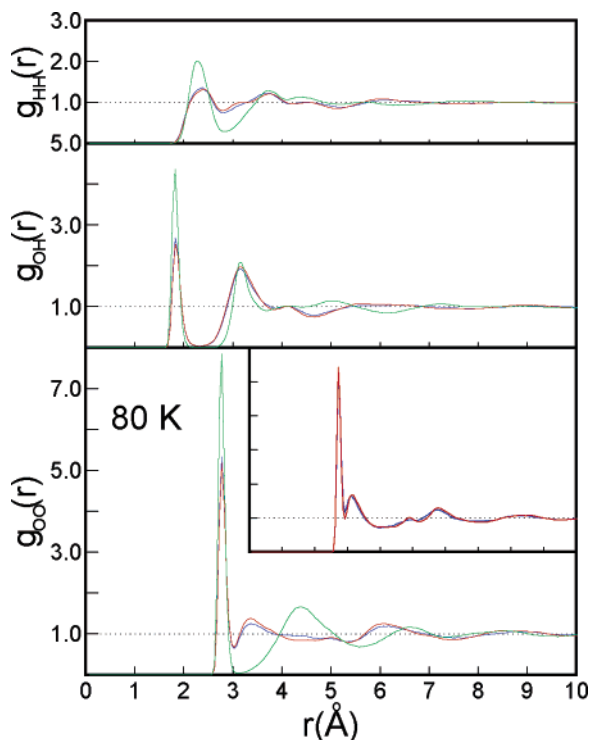

Figure 7. Oxygen−oxygen (lower panel), oxygen−hydrogen (middle panel), and hydrogen−hydrogen intermolecular pair distribution functions of LDA (green), HDA (blue), and VHDA (red) at 80 K and ambient pressure. In the inset of the lower panel we compare the HDA and VHDA $g_{OO}(r)$ at 2.0 GPa.

differences are practically absent from the oxygen−oxygen PDFs of HDA and VHDA at 2.0 GPa, where the two respective equations of state are originated. The other $g(r)$ values are almost indistinguishable through all the pressure domain.

Both experimental[27] and theoretical[12] studies agree that the first H-bond peak of the $g_{OO}(r)$ shows very minor modifications through the HDA and VHDA preparation protocols, suggesting thus that the first-shell tetrahedral cage of neighbors might be subject to insignificant, if any, structural modifications. The respective structures of HDA and VHDA can be better rational-
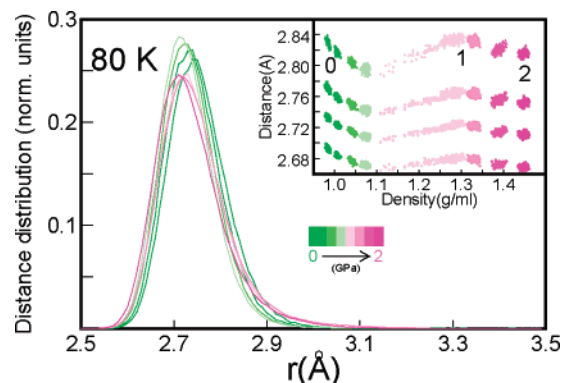

Figure 8. Normalized distance distribution of the first shell of neighbors along the upstroke at 80 K, as indicated by the color code. In the inset we report the configuration-averaged distances of each of the four neighbors as a function of the configuration density. The numbers indicate, as in Figure 3, the different stages of the simulations.

ized through the analysis of the first-shell angular rather than radial correlations,[12] and their temperature-induced difference can be explained in terms of a different behavior of the second-shell neighbors.[12,13]

IV. Neighbors and Shells

We will now analyze the structural behavior and the local topology of the three amorphous forms in terms of neighbor distributions. To this aim, we first characterize the instantaneous neighbors of each molecule at any configuration by ranking them in an increasing distance order, as done in previous studies.[12,13,28] In a perfectly ordered tetrahedral network, the first shell of coordination has 4 neighbors, and the second shell contains 12 next neighbors, namely, those from 5 to 16. We will indicate these shells in the following as I and II. The study of the amorphous ices through this analysis performed in terms of neighbors gives surprisingly many more insights on the structural properties than the simple inspection of the $g(r)$ values.

A. First Shell Neighbors. We start this part of the work by studying at first the behavior of the first shell of H-bonded neighbors. In Figure 8 we report the distance distribution of the whole shell I, namely, the neighbors 1 to 4, along the pressure upstroke from ambient pressure LDA to 2.0 GPa. The four hydrogen bonds around the central water molecule are only slightly affected by pressure, and their distribution is always peaked around the typical H-bond distance of 2.72 Å. The LDA to HDA transformation seemingly does not affect in a significant way the first-shell tetrahedral cage. However, the plot of the configuration-averaged individual lengths of the four I neighbors as a function of the instantaneous density reveals a nonmonotonic behavior. The H-bond length at first slightly shortens, as expected, upon pressure. At the LDA−HDA transformation at 0.8 GPa (stage "1") it surprisingly *increases* despite the density jump, recovering the initial LDA value, to shorten again in HDA when pressure leads to further compression (stage "2"). A possible explanation of the outward displacement will be given below.

B. Second Shell Neighbors. The second-shell (II) neighbors are on the contrary dramatically affected by the transformation, carrying the largest part of the structural rearrangement. We report in Figure 9 the distance distributions of the whole II shell (neighbors 5−16) along the upstroke from LDA and the two downstrokes to HDA and VHDA. We use here and in the following the scaled distance $r' = r \rho(t)^{1/3}$, where $\rho(t)$ is the instantaneous density, to separate the "net" displacements, specific to the transformation, from the homogeneous variation
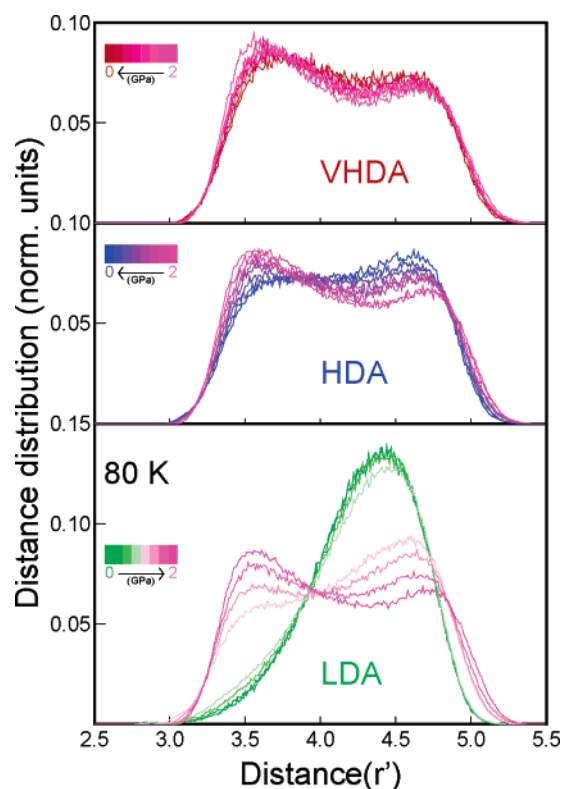
Structures of Amorphous Ice

J. Phys. Chem. B, Vol. 110, No. 8, 2006 **3599**

Figure 9. Normalized distance distributions, scaled with respect to the density (see text), of the second-shell 5−16 neighbors at 80 K. In the lower panel the upstroke curves are reported, while the middle and the upper panels refer to the HDA and the VHDA procedures, respectively. The same color code used in previous figures applies.

Figure 10. Density-scaled normalized distance distributions of the IIa (lower panel), IIb (middle panel), and IIc (upper panel) neighbors at 80 K along the upstroke. The arrows indicate the direction of the pressure increase. The same color code used in previous figures applies. In the inset we report the configuration-averaged density-scaled distance of the 5th neighbors as function of the instantaneous density. Numbers indicate the various stages of the simulations (see Figure 3).

of the distances due to the compression or expansion of the system. We also define the configuration-averaged distance r_i of the ith neighbor as the average of the density-scaled distances of all the ith neighbors of a given configuration, and thus at a given density, over the number of molecules contained in the simulation box.

The ambient pressure LDA distribution (bright green) presents a smooth single peak at about 4.4 Å that corresponds to the second peak of the oxygen−oxygen PDF. In the upstroke (lower panel) we do not observe any net displacement up to 0.6 GPa (light green). At the transformation (light magenta), the shape of the distribution changes dramatically from a single peak distribution to a double peaked one. The new peak at shorter distances becomes then more and more pronounced as pressure increases in the high-density phase. These curves clearly indicate that the second shell splits into at least two separate subgroups that behave differently under pressure. In the middle and the upper panels of the figure we show the distance distribution of the II neighbors along the downstrokes corresponding to the HDA and the VHDA procedures, respectively. In HDA, although the distributions maintain a double-peak nature, a significant shape deformation is observed as pressure decreases. In VHDA on the contrary very few changes occur along the downstroke, besides the homogeneous dilatation of the system due to the volume expansion, which is not accounted for in the figure, as explained above. This result underlines a first structural difference between the two high-density amorphous forms. In particular, the fact that in VHDA the second-shell neighbors do not show any significant net displacement in excess to the homogeneous expansion would indicate that the structure created by the high-pressure annealing at 160 K is particularly (meta)-stable throughout the entire downstroke. The noticeable HDA
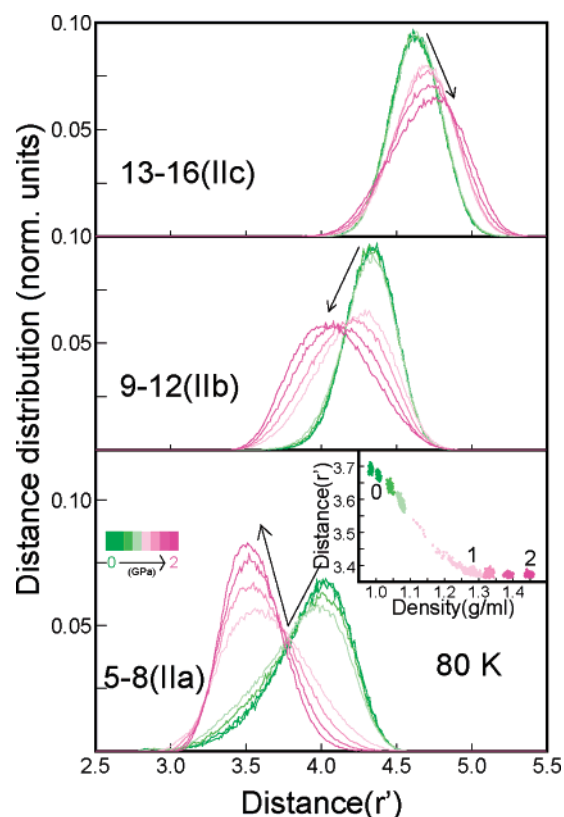
structural relaxation along the downstroke suggests instead that this latter phase is somehow not completely developed, and its high-pressure structural features are not fully maintained once pressure is released.

C. Subgroups of the Second Shell in the Upstroke. At this stage it is clear that the neighbors of shell II do not respond in the same way to pressure variations in the different amorphous forms because the shell splits into subgroups. To better discern the different mechanisms involved in the different stages of the whole process necessary to produce the amorphous ices, our analysis was developed one step further by considering these neighbors as belonging to different subgroups. In particular, we name IIa the subgroup including the neighbors 5−8, IIb the subgroup including the neighbors 9−12, and IIc the one referring to the neighbors 13−16, and we study their behavior separately. This approach allows us to single out the different structural steps corresponding to the characteristic stages of the procedure, numbered according to Figure 3.

We show in Figure 10 the density-scaled distance distributions of each of these subgroups at 80 K along the upstroke from LDA. In the lower panel the distribution of the closest non-H-bonded four neighbors suggests a two-state-like behavior, characterized by a crossover from an ambient pressure distance of about 4.0 Å to a high-pressure distance of about 3.5 Å. In the inset we report the configuration-averaged distance of the 5th neighbors (the closest non-H-bonded one) as a function of the instantaneous density, which shortens before and especially at the LDA−HDA transformation, where it then shows a plateau up to the highest simulated pressure, signaling quite clearly that a structural (meta)stable state is reached. The structural evolution
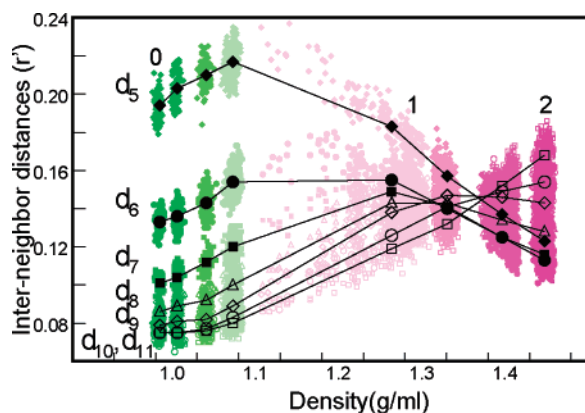
Figure 11. Configuration-averaged density-scaled difference of radial distances of consecutive IIa and IIb neighbors (see text). Full diamonds refer to d_5, full circles to d_6, full squares to d_7, empty triangles to d_8, empty diamonds to d_9, empty circles to d_{10}, and empty squares to d_{11} (see text). The same color code and numbering of Figure 3 are used. The black symbols are the simulation averages of the corresponding distributions. Lines are a guide to the eye.

Figure 12. Configuration-averaged density-scaled d_{IIab} width of the shell formed by the IIa and IIb subgroups as a function of the instantaneous density along the upstrokes at 80 K (shown with green diamonds) and at 160 K (shown with red squares). The arrow indicates the pressure increase.

along the upstroke of the other two subgroups is equally interesting. The IIb neighbors (9−12) have no net displacement at all in the low-density phase; they move instead inward *faster* than the volume contraction once in the high-density phase. However, differently from the IIa subgroups, they do not seem to reach a stable end point of their displacement within the pressure range presently studied. The IIc subgroup, which includes the neighbors 13−16, analogously shifts along the volume contraction up to 0.6 GPa. Quite surprisingly, at the HDA transformation it moves *outward*, that is, *against* the volume decrease, as illustrated in the upper panel of the figure. The behavior of these three subgroups of neighbors suggests a separation between the first subgroup, seemingly stabilized at its optimal distance, the third one, which shifts farther away, and the second subgroup, moving inward but somehow trapped "in between". A similar analysis of the HDA downstroke (not shown) confirms that the IIb subgroup is more mobile and has a larger outward displacement.

We focus now on the different behavior of the IIa and IIb subgroups, trying in particular to rationalize the formation of different local arrangements beyond the first-shell tetrahedral cage. An indicator of new pressure-induced trends is the configuration-averaged difference distances of consecutive neighbors. In other words, as explained above, we calculate for each molecule and each configuration the instantaneous distance of their 16 closest neighbors, we scale it by the density factor $\rho^{1/3}$, and we average this quantity over all the molecules to obtain a single value corresponding to the instantaneous supercell volume. We called previously r_i this configuration-averaged density-scaled distance of the ith instantaneous neighbor. The quantities $d_i = r_{i+1} - r_i$ allow us to evaluate how distant a given neighbor is from the central molecule with respect to the following one and, as a consequence, to estimate how broadly individual neighbors are distributed distancewise.

We report in Figure 11 a plot of these quantities, calculated for the IIa and IIb neighbors as a function of the density along the 80 K pressure upstroke. In LDA, d_5, d_6, and d_7 have the larger values, indicating a larger intrashell separation of the closest second-shell neighbors, which are often interstitial molecules. The other neighbors are H-bonded to the first-shell molecules, and they thus occupy relatively narrow spherical layers. When pressure is applied to LDA, the d_5, d_6, and d_7 distance differences increase more than the other ones, but once
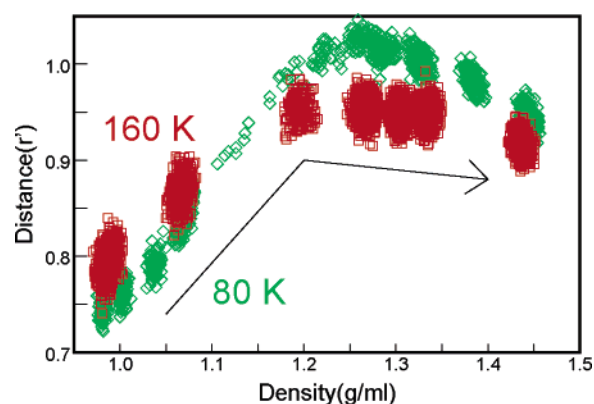
HDA is obtained they decrease steadily until they converge to a smaller value at the highest simulation pressure. On the contrary, all other distance differences increase to larger values at the end of the upstroke. This behavior is compatible with the formation, in HDA, of a "new" second shell of coordination that includes the IIa subgroup, which tend to occupy (disorderedly) the anti-tetrahedral sites just beyond the first-shell tetrahedral cage. At the same time, the former IIb neighbors become interstitial and are thus more mobile and separated from the IIa subgroup and between each other than in the LDA form.

The VHDA form, as shown in refs 12 and 13 is instead characterized by a local arrangement tending toward a random close-packed form. From the structural point of view, the IIa and IIb subgroups tend to merge and eventually form, at higher densities, a single coordination shell with the first-neighbors, whose tetrahedral geometry is then heavily distorted yet compatible with H-bonding. In the following, we will try to put on a solid footing our hypothesis on the respective structures of the high-density ices by comparing the shell thicknesses and the angular correlations of the two forms.

D. Subgroup Thickness in HDA and VHDA. We define $d_{\mathrm{IIab}} = r_{12} - r_5$ as the density-scaled thickness of the IIa and IIb neighbors combined. This quantity indicates the tendency of these subgroups to merge in a single (disordered) shell, as it is in LDA or in a rcp arrangement, or instead to split, as it would be in our postulated arrangement for HDA, where the five−eight neighbors tend to occupy the four tetrahedral voids around the first-shell cage. As mentioned before, HDA only can be obtained when the system is never heated beyond 80 K. On the contrary, VHDA develops because of the temperature annealing and can be then recovered at 80 K.

We report in Figure 12 the configuration-averaged d_{IIab} thickness as function of the instantaneous density at 80 and 160 K. At ambient pressure the thickness is larger at 160 K, as expected because of the larger disorder induced by a higher temperature. As pressure increases, the d_{IIab} thickness *increases* as well at both temperatures, due to the different pace at which the front and the back of this shell move inward. Interestingly, a larger increase, of almost 50% of the ambient pressure value, is observed at the *lower* temperature, that is, when the system transforms from LDA to HDA, the two subgroups are the farthest from each other. Beyond the transformation pressure, the IIa neighbors maintain their newfound stable positions, while the IIb subgroup moves closer. This two-step mechanism is also present at 160 K, but it is much less significant: the total
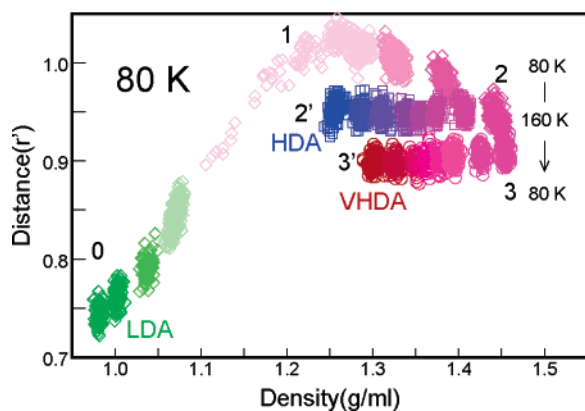
Structures of Amorphous Ice

J. Phys. Chem. B, Vol. 110, No. 8, 2006 **3601**

Figure 13. Configuration-averaged density-scaled d_{IIab} width of the shell formed by the IIa and IIb subgroups as a function of the instantaneous density along the HDA and VHDA downstrokes at 80 K. The color code and the numbering are the same as in Figure 3.
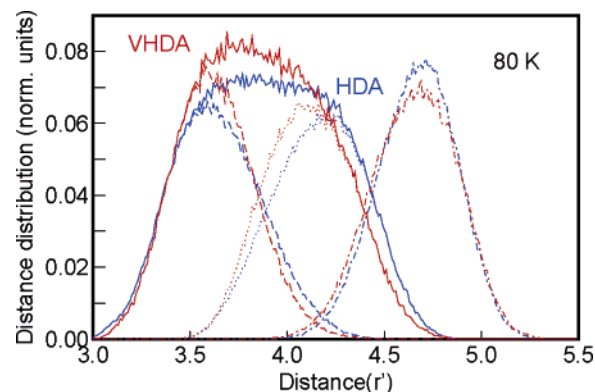

Figure 14. Density-scaled normalized distance distributions of the IIa (dashed), IIb (dotted), and IIc (dotdashed) neighbors at the end of the VHDA (red) and HDA (blue) downstrokes at 80 K. The solid lines refer to the respective superpositions of the IIa and IIb subgroups.
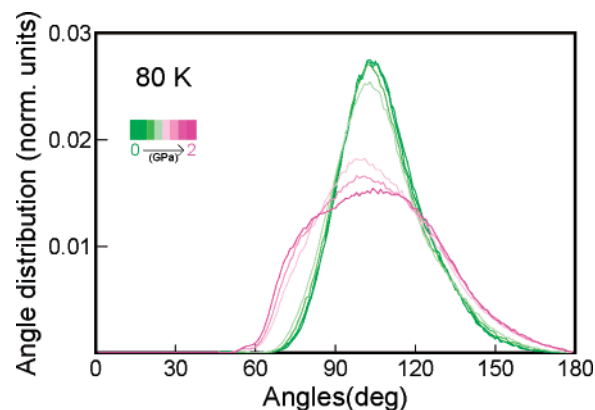

Figure 15. Normalized angular distributions of the first-shell H-bonded neighbors along the upstroke at 80 K. The same color code of Figure 3 is used.

thickness increases by only 20% at the most with respect to the ambient pressure value and does not change remarkably up to 2.0 GPa beyond the transformation pressure.

It is interesting to monitor the evolution of this quantity along the HDA and VHDA downstrokes, shown in Figure 13. The upstroke from LDA is the same as that shown in the previous figure, the different stages being numbered "0", "1", and "2". The effect of the annealing to 160 K and the subsequent cooling back to 80 K of the "2" highest-pressure sample is to reduce the total thickness d_{IIab} ("3"). As explained in ref 13, this effect is due in part to the inward net displacement of the IIb neighbors, shown in Figure 10, and in part to an unexpected *outward* displacement of the IIa subgroup. The latter result is somehow surprising because it implies that up to a distance of 3.0 Å VHDA at 2.0 GPa is slightly *less* coordinated than HDA, despite being denser, as confirmed by a close inspection of the high-pressure HDA and VHDA $g_{OO}(r)$ values shown in the inset of Figure 7.

The two downstrokes, which bring the system from the stages "2" and "3" to the stages "2′" and "3′" have a small effect on the evolution of the d_{IIab} thickness, just slightly accentuating their quantitative difference in the two cases. At ambient pressure, it is confirmed that the structural difference between the recovered high-density amorphous ices has to be found in the interplay between the second-shell 5 to 12 neighbors. In HDA the IIa and IIb subgroups are more separated since they tend to approach the central molecule at different sites in correspondence of the different stages of compression. In VHDA, the 160 K annealing provides enough kinetic energy to the IIa molecules to move from their HDA countertetrahedral sites and to merge more with the IIb neighbors. This latter mechanism proves to be the more stable one, once pressure is released. Another confirmation of this hypothesis is illustrated in Figure 14, where we plot the ambient pressure recovered density-scaled distance distributions of the IIa, IIb, and IIc neighbors, as well as the superposition of the IIa and IIb subgroups, for both HDA and VHDA. This figure shows how in VHDA the IIa and IIb neighbors are closer and form a better-defined single shell, while in HDA they stay more separate, and the IIb molecules are the ones which move farther away from the central molecule along the downstroke with respect to their VHDA counterparts.

V. Angular Correlations

In previous work[12,13,28] we have shown that knowledge of the orientational correlations of selected neighbors about the

central water molecule is crucial to infer its local structure, and in particular the structural differences in different regimes, otherwise extremely difficult to obtain on the basis of pair distribution functions only. Unfortunately, three-body terms are very difficult to extract from experimental data, while computer simulations allow us to obtain that kind of information at the atomic/molecular level. As previously shown, all the amorphous ice $g_{OO}(r)$ values have a very sharp first peak, which correctly provides, integrated up to the H-bond distance, a coordination per molecule of about 4. From this fact one might conclude that the first-shell tetrahedral cage is practically not affected by the pressure increase/decrease and the transformations to HDA and VHDA. However, we have shown[12,13] that this is not the case, and although the H-bond distances are little modified with respect to ambient conditions, the H-bond angles in VHDA distort substantially at high pressure.

We report in Figure 15 the distributions of the angles formed by couples of instantaneous H-bonded neighbors about the central molecule. The upstroke from LDA to 2.0 GPa at 80 K is shown. We observe a well-defined tetrahedral peak at low pressures which broadens once the system transforms to HDA, presenting a new shoulder at smaller angles, around 70°. Despite the pressure-induced modifications, however, the main peak indicates that the geometry is still quite tetrahedral.

Important changes occur instead when the VHDA procedure is applied. We show in Figure 16 the angular distributions of the H-bonded neighbors at 2.0 GPa for HDA at the end of the upstroke (blue), at the temperature annealing at 160 K (green), and after the system has been cooled back at 80 K, which
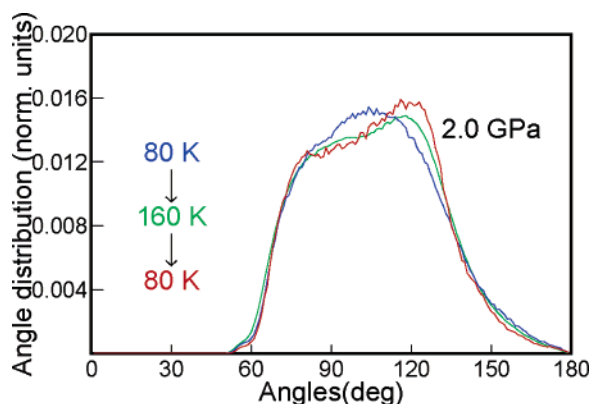
Figure 16. Normalized angular distributions of the first-shell H-bonded neighbors at 2.0 GPa. We show in blue the curve obtained at the end of the upstroke (HDA), in green the curve at 160 K, and in red the distribution after the system has been cooled back at 80 K (VHDA), as indicated in the figure.
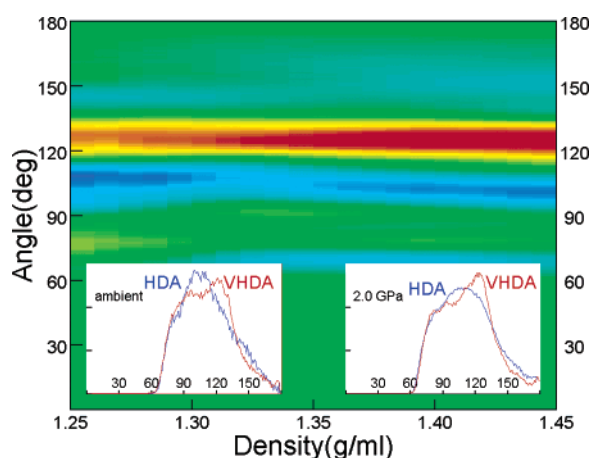

Figure 17. Difference distribution of the first-shell angles as a function of the density along the downstrokes (stages "2 → 2'" and "3 → 3'"). The red color indicates a positive VHDA−HDA difference in the respective distribution, while blue indicates a negative one. The VHDA-(HDA) distribution has been extrapolated at the low (high) end of the density axis in order to allow a comparison of the two systems along the respective downstroke equations of state. Insets: a comparison of the VHDA and HDA angular distributions at the highest (right panel) and at ambient (left panel) pressures.

corresponds thus to high-pressure VHDA (red). At this point we observe an extremely significant modification: the annealing at high temperature favors a distortion of the H-bond angles such that the main peak is not around 105° anymore, but rather around 120°. Once the system is brought back to 80 K, this new feature is enhanced; the geometry of the first-shell cage, despite a bond length quite stable, has changed from a regular (on average) tetrahedron to an irregular one.

This distortion that sets in at high pressure is then maintained throughout all the VHDA downstroke. We subtract the angular distribution of HDA along the downstroke from the analogous distribution of VHDA, and we plot the result in Figure 17 as a function of the density. This figure shows that the VHDA distributions have, at any density, a stronger feature beyond 120°, while HDA is more structured around 105°. This result indicates that in HDA the first-shell cage is rather tetrahedral along the whole process of densification and decompression, while in VHDA the annealing at 160 K triggers a major angular distortion that sets in at high pressure and is maintained even in the ambient pressure recovered sample. It is worth noting that the VHDA samples having the same density as the HDA

ones are at lower pressures, making the result shown in Figure 17 even more remarkable. The angular distortion of the tetrahedral cage has been previously explained in terms of a tendency of VHDA toward a random-close-packed local arrangement, characterized by angles tending toward close-packed typical values, such as 120° or 60°.[12] In this hypothesis the first (disordered) shell of neighbors is formed by the H-bonded I neighbors, distorted in such a way as to accommodate the non-H-bonded IIa and IIb molecules as close as possible to the central molecule.

The angular feature that differentiates VHDA from HDA fits well the above interpretation of the structural steps that are the necessary mechanisms to obtain two high-density amorphous forms. We can qualitatively summarize the characteristic stages in the formation of HDA as follows: (i) in ambient pressure LDA (stage "0") the system is characterized by a disordered tetrahedral arrangement at the first (H-bonded) and the second shells of neighbors; (ii) before and at the LDA−HDA transformation (stage "1") the IIa (five to eight) neighbors move decidedly inward, and occupy, in a statistical sense, the voids at the antitetrahedral sites in an arrangement still compatible with mostly tetrahedral angles; (iii) when HDA is further compressed (stage "2"), the IIc subgroup moves outward, and the IIb neighbors remain in a "no man's land"; (iv) when HDA is decompressed to ambient pressure (stage "2'"), the structural features are mostly maintained, except the IIb molecules which do not occupy a deep potential minimum at high pressure, and move outward when pressure is released. In the VHDA procedure, a different mechanism is observed when high-pressure HDA is annealed to 160 K: (i) the IIa neighbors have enough kinetic energy to "unlock" from the antitetrahedral sites, and move *outward*; (ii) they begin to merge with the IIb molecules, reducing their distance, to form eventually (at higher pressures) a more compact shell; (iii) in order to achieve a rcp arrangement compatible with the high density, the first-shell angles distort in order to accommodate the incoming IIa and IIb molecules; (iv) this structure is more stable and is conserved almost rigidly in recovered VHDA, besides the homogeneous volume expansion, down to ambient pressure.

VI. Conclusions

In conclusion, we have performed extensive molecular dynamics simulations to study the behavior of the three amorphous forms of ice throughout a large pressure range. We are able not only to reproduce the different amorphous forms but also to obtain new insights on their structural properties by means of an analysis in terms of neighbors, density-scaled distance distributions, and angular correlations. Our work proposes sound explanations on the mechanisms involving different subgroups of neighbors at different steps, and a strong correlation between the various structural differences observed in HDA and VHDA is provided. The former is characterized by a filling of the antitetrahedral void sites and a mostly tetrahedral angular distribution of the H-bonded neighbors, while the latter has a local structure tending toward a rcp arrangement and is characterized by a merging of the 5−12 neighbors which induces a distortion of the first-shell tetrahedral angles.

References and Notes

(1) Finney, J. L.; Hallbrucker, A.; Kohl, I.; Soper, A. K.; Bowron, D. T. *Phys. Rev. Lett.* **2002**, *88*, 225503.

Structures of Amorphous Ice

J. Phys. Chem. B, Vol. 110, No. 8, 2006 **3603**

(2) Finney, J. L.; Bowron, D. T.; Soper, A. K.; Loerting, T.; Mayer, E.; Hallbrucker, A. *Phys. Rev. Lett.* **2002**, *89*, 205503.

(3) Klug, D. D. *Nature* **2002**, *420*, 749.

(4) Klotz, S.; Hamel, G.; Loveday, J. S.; Nelmes, R. J.; Guthrie, M.; Soper, A. K. *Phys. Rev. Lett.* **2002**, *89*, 285502.

(5) Klotz, S.; Hamel, G.; Loveday, J. S.; Nelmes, R. J.; Guthrie, M. *Z. Kristallogr.* **2003**, *218*, 117.

(6) Guillot, B.; Guissani, Y. *J. Chem. Phys.* **2003**, *119*, 11740.

(7) Martoňák, R.; Donadio, D.; Parrinello, M. *Phys. Rev. Lett.* **2004**, *92*, 225702.

(8) Martoňák, R.; Donadio, D.; Parrinello, M. *J. Chem. Phys.* **2005**, *122*, 134501.

(9) Giovambattista, N.; Stanley, H. E.; Sciortino, F. *Phys. Rev. Lett.* **2003**, *91*, 115504.

(10) Giovambattista, N.; Stanley, H. E.; Sciortino, F. *Phys. Rev. Lett.* **2005**, *94*, 107803.

(11) Giovambattista, N.; Stanley, H. E.; Sciortino, F. *Phys. Rev. E* **2005**, *72*, 031510.

(12) Saitta, A. M.; Strässle, Th.; Rousse, G.; Hamel, G.; Klotz, S.; Nelmes, R. J.; Loveday, J. S. *J. Chem. Phys.* **2004**, *121*, 8430.

(13) Saitta, A. M.; Strässle, Th.; Klotz, S. Submitted, 2005.

(14) Poole, P. H.; Sciortino, F.; Essmann, U.; Stanley, H. E. *Nature* **1992**, *360*, 324.

(15) Franzese, G.; Malescio, G.; Skibinski, A.; Buldyrev, S. V.; Stanley, H. E. *Nature* **2001**, *409*, 692.

(16) Tanaka, H. *Phys. Rev. Lett.* **1998**, *80*, 113.

(17) Mishima, O.; Stanley, H. E. *Nature* **1998**, *396*, 329.

(18) Debenedetti, P. G.; Stanley, H. E. *Phys. Today* **2003**, *56*, 40.

(19) Shpakov, V. P.; Rodger, P. M.; Tse, J. S.; Klug, D. D.; Belosludov, V. R. *Phys. Rev. Lett.* **2002**, *88*, 155502.

(20) Mishima, O.; Calvert, L. D.; Whalley, E. *Nature* **1984**, *310*, 393.

(21) Tse, J. S.; Klein, M. L. *Phys. Rev. Lett.* **1987**, *58*, 1672.

(22) Mishima, O.; Calvert, L. D.; Whalley, E. *Nature* **1985**, *314*, 76.

(23) Tulk, C. A.; Benmore, C. J.; Urquidi, J.; Klug, D. D.; Neuefeind, J.; Tomberli, B.; Egelstaff, P. A. *Science* **2002**, *297*, 1320.

(24) Klotz, S.; Strässle, Th.; Loveday, J. S.; Nelmes, R. J.; Hamel, G.; Rousse, G.; Canny, B.; Chervin, J. C.; Saitta, A. M. *Phys. Rev. Lett.* **2005**, *94*, 025506.

(25) Loerting, T.; Salzmann, C.; Kohl, I.; Mayer, E.; Hallbrucker, A. *Phys. Chem. Chem. Phys.* **2001**, *3*, 5355.

(26) Jorgensen, W. L.; Chandrasekhar, J.; Madura, J. D.; Impey, R. W.; Klein, M. L. *J. Chem. Phys.* **1983**, *79*, 926.

(27) Klotz, S.; Strässle, Th.; Saitta, A. M.; Rousse, G.; Hamel, G.; Nelmes, R. J.; Loveday, J. S.; Guthrie, M. *J. Phys.: Condens. Matter* **2005**, *17*, S967.

(28) Saitta, A. M.; Datchi, F. *Phys. Rev. E (RC)* **2003**, *67*, 020201R.